SCExAO and Keck Direct Imaging Discovery of a Low-mass Companion Around the Accelerating F5 Star HIP 5319

Noah Swimmer, Thayne Currie, Sarah Steiger, G. Mirek Brandt, Timothy D. Brandt, Olivier Guyon, Masayuki Kuzuhara, Jeffrey Chilcote, Taylor Tobin, Tyler D. Groff, et al.

The Astronomical Journal, 164:152 (15pp), 2022 October https://doi.org/10.3847/1538-3881/ac85a8

SCExAO and Keck Direct Imaging Discovery of a Low-mass Companion Around the Accelerating F5 Star HIP 5319*

Noah Swimmer[1], Thayne Currie[2,3,4,5], Sarah Steiger[1], G. Mirek Brandt[1], Timothy D. Brandt[1], Olivier Guyon[2,6,7,8], Masayuki Kuzuhara[8,9], Jeffrey Chilcote[10], Taylor Tobin[10], Tyler D. Groff[11], Julien Lozi[2], John I. III Bailey[1], Alexander B. Walter[12], Neelay Fruitwala[1], Nicholas Zobrist[1], Jennifer Pearl Smith[1], Gregoire Coiffard[1], Rupert Dodkins[1], Kristina K. Davis[1], Miguel Daal[1], Bruce Bumble[12], Sebastien Vievard[2], Nour Skaf[2,13,14], Vincent Deo[2], Nemanja Jovanovic[15], Frantz Martinache[16], Motohide Tamura[8,9,17], N. Jeremy Kasdin[18], and Benjamin A. Mazin[1]
[1] Department of Physics, University of California, Santa Barbara, Santa Barbara, CA, USA; nswimmer@ucsb.edu
[2] Subaru Telescope, National Astronomical Observatory of Japan, 650 North Aóhőkű Place, Hilo, HI 96720, USA
[3] Department of Physics and Astronomy, University of Texas-San Antonio, San Antonio, TX, USA
[4] NASA-Ames Research Center, Moffett Boulevard, Moffett Field, CA, USA
[5] Eureka Scientific, 2452 Delmer Street Suite 100, Oakland, CA, USA
[6] Steward Observatory, The University of Arizona, Tucson, AZ 85721, USA
[7] College of Optical Sciences, University of Arizona, Tucson, AZ 85721, USA
[8] Astrobiology Center, 2-21-1, Osawa, Mitaka, Tokyo, 181-8588, Japan
[9] National Astronomical Observatory of Japan, 2-21-2, Osawa, Mitaka, Tokyo 181-8588, Japan
[10] Department of Physics, University of Notre Dame, South Bend, IN, USA
[11] NASA-Goddard Space Flight Center, Greenbelt, MD, USA
[12] Jet Propulsion Laboratory, California Institute of Technology, Pasadena, CA 91125, USA
[13] LESIA, Observatoire de Paris, Univ. PSL, CNRS, Sorbonne Univ., Univ. de Paris, 5 pl. Jules Janssen, F-92195 Meudon, France
[14] Department of Physics and Astronomy, University College London, London, UK
[15] Department of Astronomy, California Institute of Technology, 1200 E. California Boulevard, Pasadena, CA 91125, USA
[16] Université Côte d'Azur, Observatoire de la Côte d'Azur, CNRS, Laboratoire Lagrange, France
[17] Department of Astronomy, Graduate School of Science, The University of Tokyo, 7-3-1, Hongo, Bunkyo-ku, Tokyo, 113-0033, Japan
[18] University of San Francisco, San Francisco, CA 94118, USA
Received 2022 April 7; revised 2022 July 19; accepted 2022 July 30; published 2022 September 21

Abstract

We present the direct imaging discovery of a low-mass companion to the nearby accelerating F star, HIP 5319, using SCExAO coupled with the CHARIS, VAMPIRES, and MEC instruments in addition to Keck/NIRC2 imaging. CHARIS *JHK* (1.1–2.4 μm) spectroscopic data combined with VAMPIRES 750 nm, MEC *Y*, and NIRC2 L_p photometry is best matched by an M3–M7 object with an effective temperature of $T = 3200$ K and surface gravity log $(g) = 5.5$. Using the relative astrometry for HIP 5319 B from CHARIS and NIRC2, and absolute astrometry for the primary from Gaia and Hipparcos, and adopting a log-normal prior assumption for the companion mass, we measure a dynamical mass for HIP 5319 B of $31^{+35}_{-11} M_J$, a semimajor axis of $18.6^{+10}_{-4.1}$ au, an inclination of $69.4^{+5.6}_{-15}$ degrees, and an eccentricity of $0.42^{+0.39}_{-0.29}$. However, using an alternate prior for our dynamical model yields a much higher mass of $128^{+127}_{-88} M_J$. Using data taken with the LCOGT NRES instrument we also show that the primary HIP 5319 A is a single star in contrast to previous characterizations of the system as a spectroscopic binary. This work underscores the importance of assumed priors in dynamical models for companions detected with imaging and astrometry, and the need to have an updated inventory of system measurements.

Unified Astronomy Thesaurus concepts: Direct imaging (387); Low mass stars (2050); Radial velocity (1332); Exoplanet astronomy (486)

1. Introduction

Over the past two decades, both facility adaptive optics (AO) systems and now extreme AO systems have provided numerous images of planets and low-mass brown dwarfs around nearby stars (e.g., Marois et al. 2008, 2010; Thalmann et al. 2009; Carson et al. 2013; Kuzuhara et al. 2013; Currie et al. 2014; Macintosh et al. 2015; Konopacky et al. 2016; Chauvin et al. 2017; Cheetham et al. 2018; Keppler et al. 2018; Currie et al. 2022c). The majority of discoveries draw from *blind* (or "unbiased") surveys, where targets are selected based on age and distance (e.g., Desidera et al. 2021). However, these same surveys show that occurrence rates of detectable moderate-to-wide-separation planets and brown-dwarf companions is low, ∼a few percent around FGK stars (Nielsen et al. 2019; Vigan et al. 2021; Currie et al. 2022a).

Recent work has demonstrated the success instead of dynamics-selected direct imaging surveys, specifically using precision astrometry from the Gaia and Hipparcos satellites in the Hipparcos–Gaia Catalog of Accelerations (HGCA; Brandt 2021) to identify stars showing a proper motion anomaly—i.e., an astrometric acceleration—likely due to an

* Based in part on data collected at Subaru Telescope, which is operated by the National Astronomical Observatory of Japan. Some of the data presented herein were obtained at the W. M. Keck Observatory, which is operated as a scientific partnership among the California Institute of Technology, the University of California and the National Aeronautics and Space Administration. The Observatory was made possible by the generous financial support of the W. M. Keck Foundation. This work makes use of observations from the Las Cumbres Observatory global telescope network (LCOGT).

unseen low-mass companion (van Leeuwen 2007; Brown et al. 2018; Brandt 2021; Gaia Collaboration et al. 2021). Direct imaging of targets showing an acceleration from HGCA have revealed white dwarfs (Bonavita et al. 2020), low-mass stars (Chilcote et al. 2021; Steiger et al. 2021), moderate-to-low-mass brown dwarfs (Currie et al. 2020; Bowler et al. 2021; Bonavita et al. 2022; Kuzuhara et al. 2022), and now planets (Currie et al. 2022b).

Jointly analyzing absolute astrometry of the star from HGCA and relative astrometry of the imaged companion with Markov chain Monte Carlo (MCMC) codes like `orvara` (Brandt et al. 2021) can provide strong constraints on the companion's dynamical mass and orbit (e.g., Brandt et al. 2021). To derive these constraints, MCMC codes require input priors for the orbital parameters, primary mass, and companion mass(es). Typical orbital priors include a log-normal distribution in semimajor axis ($p(a) \propto 1/a$), uniform prior in inclination ($p(i) \propto \sin(i)$), Gaussian prior in primary mass, and log-normal prior in companion mass ($p(M_2) \propto 1/M_2$) (e.g., Kuzuhara et al. 2022).

While the above orbital priors are long regarded as standard in MCMC modeling (e.g., Blunt et al. 2020), the most appropriate companion prior may differ. The initial mass function for companions near the substellar to stellar boundary exhibits a more Gaussian-like distribution (e.g., Chabrier 2003), i.e., a turnover in the mass function near the hydrogen-burning limit. Ancillary system properties—e.g., age, primary and companion spectral type, etc.—also are often used to inform adopted priors but may derive from heterogeneously-sourced data.

Here, we report the direct imaging discovery of HIP 5319 B: a low-mass—potentially substellar—companion around the F-type star HIP 5319 A using the Subaru Coronagraphic Extreme Adaptive Optics system (SCExAO; Jovanovic et al. 2015; Ahn et al. 2021) coupled with the MKID Exoplanet Camera (MEC; Walter et al. 2020), the Visible Aperture Masking Polarimetric Imager for Resolved Exoplanetary Structures (VAMPIRES; Norris et al. 2015), the Coronagraphic High Angular Resolution Imaging Spectrograph (CHARIS; Groff et al. 2016), and the NIRC2 camera on the Keck II telescope. HIP 5319 B illustrates the sensitivity of adopted priors for companion mass for parameters derived from jointly modeling direct imaging and astrometric data and the need to verify ancillary information about the system—e.g., binarity, age, rotation—in direct imaging + astrometric surveys.

2. Stellar Properties and Observations

2.1. HIP 5319 A Basic Properties

HIP 5319 (*78 Psc) is an F5IV spectral class star (Boro Saikia et al. 2018) at $d = 42.93 \pm 0.06$ pc (Prusti et al. 2016; Brown et al. 2018). Banyan-Σ (Gagné et al. 2018) shows no evidence that the system is a member of any moving group or young association. It has previously been identified as an RS CVn binary star by Fleming et al. (1989), who measured a projected rotation rate of $v\sin(i) = 68 \pm 20.5\,\mathrm{km\,s^{-1}}$ and x-ray luminosity of $L_x = 9.2 \pm 3.7 \times 10^{28}$ erg s^{-1}.

2.1.1. System Age

Evidence informing the HIP 5319 system's age is complex. On one hand, HIP 5319 has an extreme level of chromospheric activity ($\log(R'_{HK}) = -4.016$) as measured by Calcium II H and K lines, which tracks the strength of the emission at the cores of the two lines (Boro Saikia et al. 2018). The chromospheric index easily exceeds values for stars in the Pleiades and Hyades associations and is comparable or higher to the stars in the Scorpius–Centaurus association (Mamajek & Hillenbrand 2008; Pecaut & Mamajek 2013). Its Hertzsprung–Russell diagram position in Gaia color–magnitude space (M_G versus $G_{BP} - G_{RP} = 2.97, 0.54$) lies between the Pleiades and Hyades, which is consistent with either a main-sequence star between 115 and ∼800 Myr, respectively (Gossage et al. 2018), or a pre-main-sequence star much younger than the Pleiades. Based on its activity, Stanford-Moore et al. (2020) estimate a young age of $75^{+492}_{-63.5}$ Myr.

HIP 5319 was also observed by the Transiting Exoplanet Survey Satellite (Ricker et al. 2015) and has 2 minute cadence photometry for one sector. This observation may be too short to show spots reliably, but it does show pulsations with a period of just less than 1 day.[19] It was also observed once by the International Ultraviolet Explorer (IUE) during IUE Program ID: CB401 (Stellar Chromospheres; Blanco et al. 1982). In the spectrum from IUE,[20] HIP 5319 A shows strong emission from the Lyman α line. These two data points show signs that the primary might be chromospherically active, though follow-up observation is required to determine the nature of this activity.

On the other hand, RS CVn binaries—of which HIP 5319 is claimed to be an example—typically have orbital periods less than 14 days and show high levels of chromospheric activity via strong emission in Calcium II H and K lines, and have a hotter component of spectral type F or G (Montesinos et al. 1988). Multiple sources have reported $v\sin(i)$ values with significant scatter, which may suggest binarity: $125\,\mathrm{km\,s^{-1}}$ (Danziger & Faber 1972), $68 \pm 20.5\,\mathrm{km\,s^{-1}}$ (Fleming et al. 1989), $36.4 \pm 4.8\,\mathrm{km\,s^{-1}}$ (de Medeiros & Mayor 1999), $35\,\mathrm{km\,s^{-1}}$ (Nordström et al. 2004), and $41.5\,\mathrm{km\,s^{-1}}$ (Głębocki & Gnaciński 2005; Glebocki & Gnacinski 2005). The fractional X-ray luminosity of the star is $\log(L_x/L_{bol}) \sim -4.9$ (Gioia et al. 1990; Favata et al. 1995), almost two orders of magnitude less than a typical pre-main-sequence star, which would have values of $\log(L_x/L_{bol}) \sim -3.2$ for fractional X-ray luminosity (Preibisch et al. 2005), respectively. Other authors have estimate the age of the star using isochrones and have found values of $1.6^{+0.3}_{-0.4}$ Gyr (Holmberg et al. 2009) and 1.07–1.23 Gyr using Padova and BASTI models (Casagrande et al. 2011).

Ultimately, the conflicting identifications of the HIP 5319 primary as either a young, chromospherically active star or an older star whose Ca II HK emission is due to a close binary will have significant implication on the understanding of the stellar system and interpretation of any of its companions' properties. If there is not significant HK emission and little evidence of binarity then the higher age estimate is likely the correct one, which will anchor the interpretation of its companion. Therefore, in addition to performing a direct imaging search for such a binary companion, a spectroscopic study of the primary with a high-resolution spectrograph is necessary to disentangle the possible identities of the star and settle on the correct interpretation. This will be discussed further in Sections 3.1 and 3.2.

2.1.2. Evidence for an Astrometric Acceleration

The Hipparcos–Gaia Catalog of Accelerations reports a $\chi^2 = 171.04$, evidence of a 12.9σ significant acceleration of the primary with 2 degrees of freedom (Brandt 2021). The

[19] Accessed via https://mast.stsci.edu/portal/Mashup/Clients/Mast/Portal.html.
[20] Accessed via https://archive.stsci.edu/iue/obtaining.html.

Table 1
HIP 5319 Observing Log

UT Date	Instrument	coronagraph	Seeing (″)	Passband	λ (μm)[a]	t_{exp} (s)	N_{exp}	ΔPA (°)	Post-processing Strategy
20200731	SCExAO/CHARIS	Lyot	0.4–0.6	*JHK*	1.16–2.37	30.98	14	5.3	RDI-KLIP
⋯	SCExAO/MEC	Lyot	⋯	*Y*	0.95–1.12	5.0-10.0	61[b]	4.6	none
20210911	SCExAO/CHARIS	Lyot	0.5–0.6	*JHK*	1.16–2.37	30.98	8 (32)[c]	9.9	none
⋯	SCExAO/VAMPIRES	⋯	⋯	750 nm	0.75	12.8	48	11.2	ADI-ALOCI
20220115	Keck/NIRC2	none	0.6	L_p	3.78	30	30	9.1	RDI-KLIP
20220119	SCExAO/MEC	Lyot	0.7	*YJ*	0.95–1.4	15	49	3.8	none

Note. (a) For CHARIS and MEC data, this column refers to the wavelength range. For broadband imaging data, it refers to the central wavelength. (b) Total integration time is 430 s. (c) In total, we obtained 32 exposures but only 8 were retained due to substantial PSF core splitting from low-wind effect.

statistically significant acceleration of HIP 5319 is suggestive of the presence of a previously unseen low-mass companion at a $\gtrsim$10 au scale. HIP 5319 was not known to have a wide-separation binary companion that could plausibly be source of this acceleration.

Therefore we chose to observe this target in an attempt to uncover any previously unimaged low-mass companions around this accelerating star, following a similar method of target selection as in Currie et al. (2020) and Steiger et al. (2021).

2.2. Observations and Data Reduction

HIP 5319 was observed during three different epochs in 2020 July, 2021 September, and 2022 January at the Subaru Telescope on Maunakea using SCExAO coupled with the CHARIS, MEC, and VAMPIRES instruments. During these epochs, the seeing conditions at the Subaru Telescope ranged between θ_V = 0.″4–0.″7. Observing conditions were photometric each night.[21] It was also observed for a fourth epoch in 2022 January at the W. M. Keck Observatory on Maunakea using the NIRC2 instrument coupled with the Keck Adaptive Optics system. The seeing during this epoch was $\theta_V = 0.''6$. The observations from these runs are summarized in Table 1.

All of the observations were taken with SCExAO using its "vertical angle"/pupil-tracking mode which enables ADI (Marois et al. 2006). Each set of data also used the Lyot coronagraph (0.″113 radius occulting mask) to suppress light from the primary star. The data in both epochs also utilized satellite spots for precise astrometric and spectrophotometric calibration (Jovanovic et al. 2015; Currie et al. 2018a).

The MEC data in 2020 July was taken in *Y* band (0.95–1.12 μm) with a spectral resolution $\mathcal{R} \sim 4.0$ simultaneously with CHARIS broadband data. The CHARIS data in both epochs was taken in its low-resolution broadband mode covering *JHK* passbands (1.16–2.37 μm) at $\mathcal{R} \sim 18$. VAMPIRES data were taken at 750 nm concurrently with CHARIS in broadband mode in 2021 September. In addition to the SCExAO observing mode allowing for ADI, the CHARIS spectral coverage enables SDI (Marois et al. 2000). The NIRC2 data were taken in the L_p filter (λ_c= 3.78 μm). Later in 2022 January more MEC data were taken covering *YJ* bands (0.95–1.14 μm) with resolution $\mathcal{R} \sim 2.4$.

HIP 5319 was also observed for spectroscopic characterization of the primary during 2022 January and February. Spectra were obtained using the Network of Robotic Echelle Spectrographs (NRES) 1 m instrument operated by the Las Cumbres Observatory global telescope network (LCOGT; Brown et al. 2013) at the Wise Observatory in Mitzpe Ramon, Israel over the course of nine nights from 2022 January 20 to February 12. These were taken using fiber-fed optical (0.38–0.86 μm) echelle spectrographs which have a spectral resolution of $\mathcal{R} \approx 50{,}000$ and a signal-to-noise ratio (S/N) > 200 for all but two of the spectra. The spectroscopic observations from the LCOGT NRES instrument are summarized in Table 2.

Table 2
HIP 5319 LCOGT Observing Log[a]

BJD	t_{exp} (s)	S/N[b]	RV (km s^{-1})	$v$sin(i) (km s^{-1})
2459600.268	1000	230	17.30 ± 1.80	95.24 ± 1.65
2459601.266	⋯	237	17.94 ± 1.59	95.63 ± 1.59
2459605.194	1500	316	18.12 ± 1.81	93.37 ± 1.64
2459607.221	1000	227	16.07 ± 1.23	95.89 ± 1.64
2459608.227	⋯	246	16.18 ± 1.13	94.50 ± 1.64
2459608.246	1500	218	14.04 ± 1.28	94.49 ± 1.64
2459609.221	⋯	281	17.31 ± 2.56	92.69 ± 1.60
2459609.202[c]	1000	227	⋯	⋯
2459610.220	1500	277	17.24 ± 1.41	94.51 ± 1.61
2459610.242[d]	1000	249	⋯	⋯
2459612.185	⋯	189	16.31 ± 1.88	93.08 ± 1.67
2459614.192	⋯	170	16.53 ± 1.39	92.68 ± 1.79
2459622.193	⋯	256	17.63 ± 2.29	94.50 ± 1.60
2459623.194	⋯	203	18.41 ± 2.63	92.22 ± 1.76

Notes. BJD 2459600 corresponds to UT Date 20220120.
[a] All data taken from λ = 0.38–0.86 μ m.
[b] Values reported are S/N per resolution element at 0.518 μm.
[c] There are two spectra taken on 2459609. Both spectra are combined to measure RV and $v$sin(i) signals.
[d] There are two spectra taken on 2459610. Both spectra are combined to measure RV and $v$sin(i) signals.

2.2.1. CHARIS

We extracted CHARIS data cubes from the raw data using the standard CHARIS pipeline (Brandt et al. 2017) to perform basic reduction steps—image registration and spectrophotometric calibration. We did not obtain sky frames for sky subtraction. For spectrophotometric calibration, we adopted a Kurucz stellar atmosphere model appropriate for an F5IV star. HIP 5319 B is easily visible in the raw data for both CHARIS observations, but the 2021 September data suffered chronic PSF splitting due to a low-wind effect, leaving us with only eight exposures totaling just over 4 minutes of integration time. The 2020 July data were stable; thus, we consider the 2021 September data only for astrometry and employ PSF subtraction to yield a high-quality spectrum for the 2020 July data.

[21] The observing conditions during the 2022 January epoch were photometric, but due to instrument constraints there was no appropriate energy calibration of the MEC instrument, disallowing the measurement of a meaningful photometric data point.

To subtract the PSF in the 2020 July data, we followed previous steps in Steiger et al. (2021), using a full-frame implementation of reference star differential imaging (RDI) using the Karhunen–Loève Image Projection (KLIP; Soummer et al. 2012) algorithm, as in Currie et al. (2019). Since the companion around HIP 5319 was easily visible, we adopted a conservative approach, truncating the KLIP basis set at one mode (KL = 1). We corrected for minor throughput losses using KLIP forward modeling as in Pueyo (2016).

2.2.2. VAMPIRES

For VAMPIRES data, we subtracted dark frames and then aligned each subexposure within the 12.8 s data cubes, removing outliers. Subsequent steps used the general purpose high-contrast ADI broadband imaging pipeline from Currie et al. (2011). To calibrate the VAMPIRES photometry an appropriate PHOENIX model stellar spectrum[22] (Husser et al. 2013) for an F5IV star was obtained and then normalized to the reported *J*-band flux value for the HIP 5319 primary from the Two Micron All Sky Survey (Skrutskie et al. 2006). Once the model stellar spectrum had been calibrated, the flux density at 750 nm was found to be 13.18 Jy. For PSF subtraction, we found the best results with a full-frame implementation of ALOCI (Currie et al. 2012, 2015). Following Currie et al. (2018a), we used forward modeling to correct for throughput losses.

2.2.3. MEC

Y-band images were created using the MKID Science Data Pipeline (Steiger et al. 2022) to apply calibrations to the raw MEC data that include cold-, dead-, and hot-pixel masking, along with wavelength, astrometric, and spectrophotometric calibrations. There was no PSF subtraction performed for the data from MEC in this analysis.

The spectrophotometric calibration follows the treatment in Steiger et al. (2021) in which the flux from the elongated satellite spots in the image was measured using a "racetrack" aperture (Millar-Blanchaer et al. 2016) before being converted to the stellar flux behind the coronagraph using the relationship between satellite spot contrast and bandpass described in Currie et al. (2018a). The stellar flux in the observation is then matched to the calibrated model spectrum from Section 2.2.2 to find a spectrophotometric solution, which is applied to the image to convert from counts per second units to units of flux density.

2.2.4. NIRC2

Our reduction steps followed ones outlined in Steiger et al. (2021). Briefly, we used a well-tested general purpose high-contrast ADI broadband imaging pipeline (Currie et al. 2011) to perform basic processing, including sky subtraction, image registration, and photometric calibration. To subtract the PSF, we used a full-frame implementation of RDI using the KLIP (Soummer et al. 2012) algorithm as in Currie et al. (2019). The star BD+54 408 was used as a reference PSF. Following Pueyo (2016), we used forward modeling to correct for throughput losses.

[22] http://phoenix.astro.physik.uni-goettingen.de/

2.2.5. NRES

All spectra from the LCOGT 1-m NRES observations are automatically reduced using the BANZAI-NRES data reduction pipeline.[23] After reduction, each spectrum was fit to the same F5IV star model stellar spectrum used in Sections 2.2.2 and 2.2.3 and both RV and $v\sin(i)$ values for the primary were subsequently extracted using the Hα and Hβ spectral lines (nominally at $\lambda_\alpha = 0.656\,\mu$m and $\lambda_\beta = 0.486\,\mu$m), which are shown in Table 2.

The RV and $v\sin(i)$ values were calculated iteratively. For each spectra, an RV offset was fit via cross correlation with a PHOENIX model spectrum (the same that was used in Sections 2.2.2 and 2.2.3 for VAMPIRES and MEC calibration) convolved to a first guess $v\sin(i)$ of 100 km s^{-1}. At that RV offset a $v\sin(i)$ is then calculated by minimizing χ^2 between the model and NRES spectra, convolving over a grid of $v\sin(i)$ values between 50 and 150 km s^{-1}. This process is then iterated until the values for RV and $v\sin(i)$ converge, meaning that the scatter between the value of the most recent iteration and the previous is less than the formal error. The formal errors on the $v\sin(i)$ values are calculated using standard χ^2 statistics. The formal error on the RV values are from the 1σ confidence interval of the bootstrap probability density of the radial velocity.

2.3. Detections

Over all epochs, the seeing conditions and data quality led to strong detections of the companion in each observing data set. To calculate flux density measurements in each channel, we performed aperture photometry sized to 1 λ/D. The S/N was calculated in the standard fashion, replacing each pixel with the sum within an aperture, computing the robust standard deviation of these summed pixels as a function of angular separation and dividing by the stellar flux (Marois et al. 2008; Currie et al. 2011). Our spectrophotometric errors and S/N values consider finite-element corrections (Mawet et al. 2014). S/N values range from 15.7 in the *Y* band image from MEC to 763 in the broadband wavelength-collapsed CHARIS data taken in 2022 January and 2020 July, respectively. Following previous work, we use the IDL function cntrd.pro to estimate companion centroids: the error budget considers the intrinsic S/N of the detection, uncertainties in the plate scale and north position angle, and astrometric biases from processing (Pueyo 2016).

In the 2020 July data, HIP 5319 B is located at [E,N]″ = [0.″124, 0.″311] ± [0.″004, 0.″004] and [0.″119, 0.″314] ± [0.″010, 0.″010] in the CHARIS and MEC data, respectively. The errors in position take into account centroiding precision, the uncertainty in true north position angle, and pixel scale of each instrument following Currie et al. (2020).

The 2021 September data from CHARIS and VAMPIRES show the companion at [E,N]″ = [0.″133, 0.″287] ± [0.″004, 0.″004] and [0.″132, 0.″287] ± [0.″004, 0.″004]. The measurements taken by multiple instruments in both epochs are the same within error. The detections from each instrument are shown in Figure 1.

In 2022 January, the NIRC2 and MEC data show the companion at [E,N]″ = [0.″133, 0.″275] ± [0.″003, 0.″003] and [0.″131, 0.″273] ± [0.″010, 0.″010], where the MEC data were taken 4 days after the NIRC2 observations.

[23] Accessible at https://github.com/lcogt/banzai-nres.

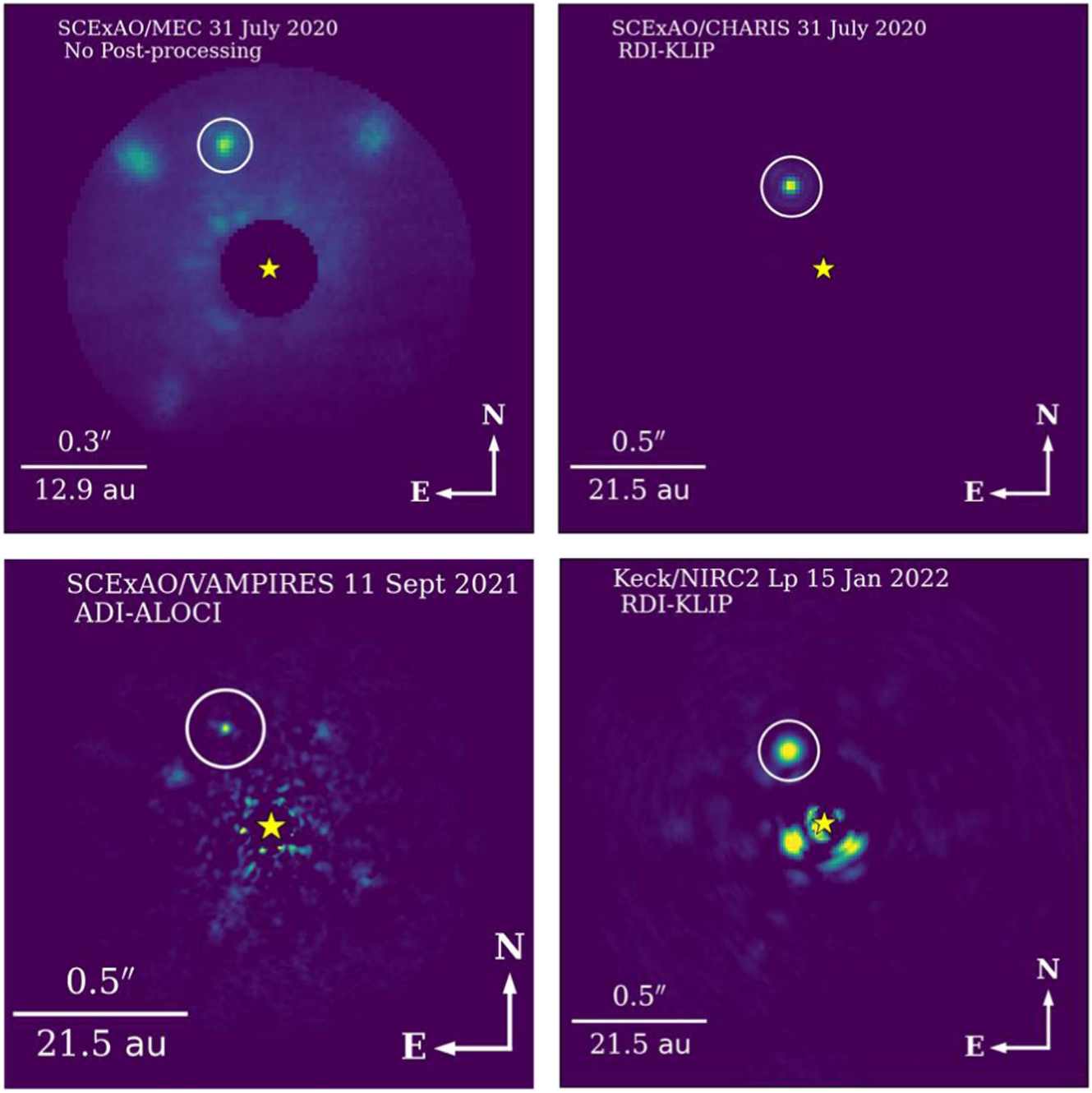

Figure 1. Detection of HIP 5319 B from SCExAO coupled with MEC, CHARIS, and VAMPIRES, and Keck II Adaptive optics coupled with NIRC2. The MEC and VAMPIRES images retain some residual signal from satellite spots used for spectrophotometric and astrometric calibration. In MEC data, these spots appear with different brightnesses due to vignetting from the optics in MEC and dead pixels on the array, both of which have since been corrected. The NIRC2 image also retains some signal from the primary that was not removed by RDI-KLIP. The CHARIS data do retain some residual signal although the signal is so low that it cannot be seen without drastically lowering the maximum value of intensity in the image and saturating the PSF.

Based on the proper motion of the primary between 2020 July and 2021 September, a background star would have moved northwest by $\sim[-0\farcs23, 0\farcs03]$, which is inconsistent with the measured companion offset of $[0\farcs009, -0\farcs024]$.

In standard Maunakea Observatory filters, the photometry for HIP 5319 B from the CHARIS broadband data is found to be $J = 10.88 \pm 0.02$, $H = 10.31 \pm 0.02$, and $K = 10.07 \pm 0.03$ from the 2020 July data. These values are within 1σ uncertainty for H and K band and 2σ uncertainty for the measured J-band photometry points measured in 2021 September. The MEC Y-band photometry is found to be $Y = 11.3 \pm 0.1$, and VAMPIRES measured a flux density of 18.83 ± 0.83 mJy at 750 nm.[24] Note that these measurements do not consider an absolute spectrophotometric uncertainty—i.e., a multiplicative factor in flux density, additive in magnitude—of 5% due to uncertainties in the mapping between the deformable mirror modulation amplitude used to produce satellite spots and the resulting spot contrast at our fiducial wavelength of 1.55 μm (Currie et al. 2018b). In the Keck II Telescope filters the

[24] For further discussion of the VAMPIRES photometry at 750 nm and its conversion to a pseudomagnitude see Section 3.3.

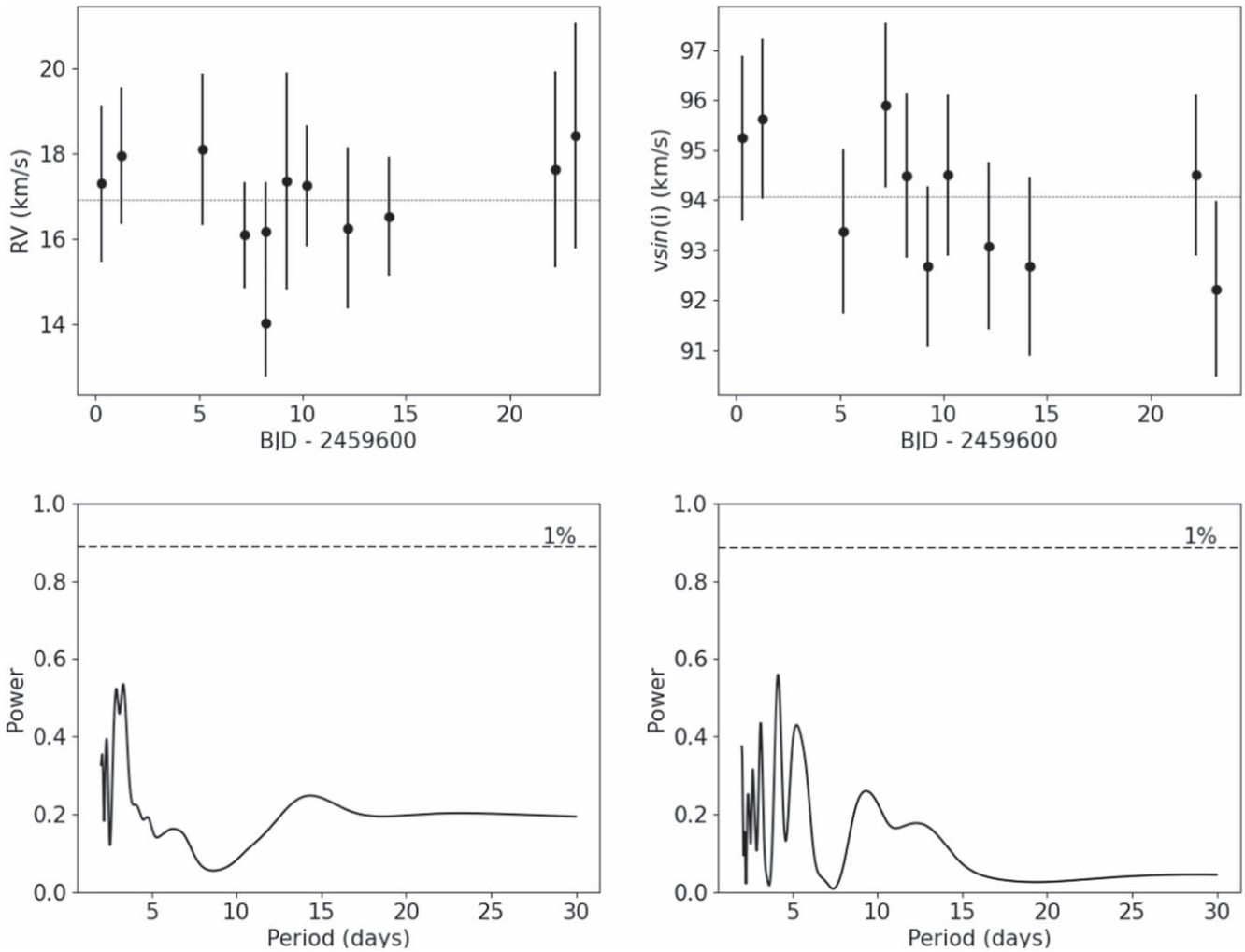

Figure 2. (Top) Radial-velocity (left) and $v\sin(i)$ (right) values measured for HIP 5319A. The dotted lines in each panel are the best-fit constant velocity to the data, where RV = 16.71 km s^{-1} and $v\sin(i)$ = 94.21 km s^{-1}. Neither metric shows either significant variation in time or obvious periodicity. (Bottom) Periodograms of the residuals from the radial-velocity (left) and $v\sin(i)$ (right) values. The residuals for each metric are calculated by taking the measured data and subtracting the best-fit constant velocity. The false-alarm probability of 1%, calculated using bootstrap randomization, is shown by the dashed lines.

photometry from the NIRC2 data is found to be $L_p = 9.39 \pm 0.07$. The full summary of the HIP 5319 B detection significance, astrometry, and photometry is found in Table 3.

3. Analysis

3.1. Characterization of HIP 5319 A as a Single Star

Before the properties of the companion can be determined it is first necessary to identify whether the primary is a binary or single star. Using the RV and $v\sin(i)$ values we look for periodic variations in time to help infer the presence of a companion or lack thereof. The top panels in Figure 2 show the measured values of each quantity and the best fit to a constant velocity.

The search for $v\sin(i)$ is motivated due to large scatter in this quantity's previously reported values in the literature, which range from 35 km s^{-1} (Nordström et al. 2004) to 125 km s^{-1} (Danziger & Faber 1972) at the low and high ends, respectively. In the collection of stars discussed in Fleming et al. (1989) HIP 5319 has the greatest uncertainty on its $v\sin(i)$ value, nearly double the next highest uncertainty and almost q1/3 of its reported rotation rate. This wide scatter in reported rotation rates along with the high uncertainties reported on these measurements led us to consider whether there may be a binary companion, where both objects contribute to the spectrum whose individual signals have not been teased out. Since we can obtain $v\sin(i)$ from the NRES spectra we use this opportunity to search for any signal in the data which may indicate the presence of a second, unseen companion contaminating the signal from the primary star.

The bottom panels in Figure 2 show periodograms of the residuals from the RV and $v\sin(i)$ data. The peak values of each periodogram are 0.559 and 0.535, respectively. Assuming there is no periodic signal in the data, this means that a peak this high or higher will be seen 79.6% of the time in the RV data and 67.6% of the time in the $v\sin(i)$ data. Also shown are the required peak heights to attain a 1% false-alarm probability for each measurement. For the radial-velocity data a peak would have to have a power of 0.888 to attain a false-alarm probability below 1%, while the $v\sin(i)$ peak would need to have a power of 0.894 to meet the same criterion. The height of the two peaks from the periodograms combined with the high peak values needed to attain a 1% false-alarm probability demonstrate that there is no obvious periodic signal, meaning the time series RV and $v\sin(i)$ data are

Table 3
HIP 5319 B Detection Significance, Astrometry, and Photometry

UT Date	Instrument	Passband	S/N	[E,N](″)	Photometry
20200731	SCExAO/CHARIS	*JHK*	763	[0.124, 0.311] ± [0.004, 0.004]	$J = 10.88 \pm 0.02$, $H = 10.31 \pm 0.02$, $K = 10.07 \pm 0.03$
20200731	SCExAO/MEC	*Y*	22.8	[0.119, 0.314] ± [0.010, 0.010]	$Y = 11.3 \pm 0.1$
20210911	SCExAO/CHARIS	*JHK*	48	[0.133, 0.287] ± [0.004, 0.004]	$J = 11.02 \pm 0.06$, $H = 10.38 \pm 0.05$, $K = 10.09 \pm 0.06$
20210911	SCExAO/VAMPIRES	750 nm	23	[0.132, 0.287] ± [0.004, 0.004]	18.83 mJy ± 0.83 mJy
20220115	Keck/NIRC2	L_p	16.1	[0.133, 0.275] ± [0.003, 0.003]	$L_p = 9.39 \pm 0.067$
20220119	SCExAO/MEC	*YJ*	15.7	[0.131, 0.273] ± [0.010, 0.010]	⋯

Note. There is no photometry point measured during the 20220119 SCExAO/MEC observation. The CHARIS photometry do not consider an additional 0.05 mag uncertainty drawn from the mapping between the deformable mirror modulation amplitude (used to produce satellite spots used for spectrophotometric calibration) and the resulting satellite spot contrast with respect to the star.

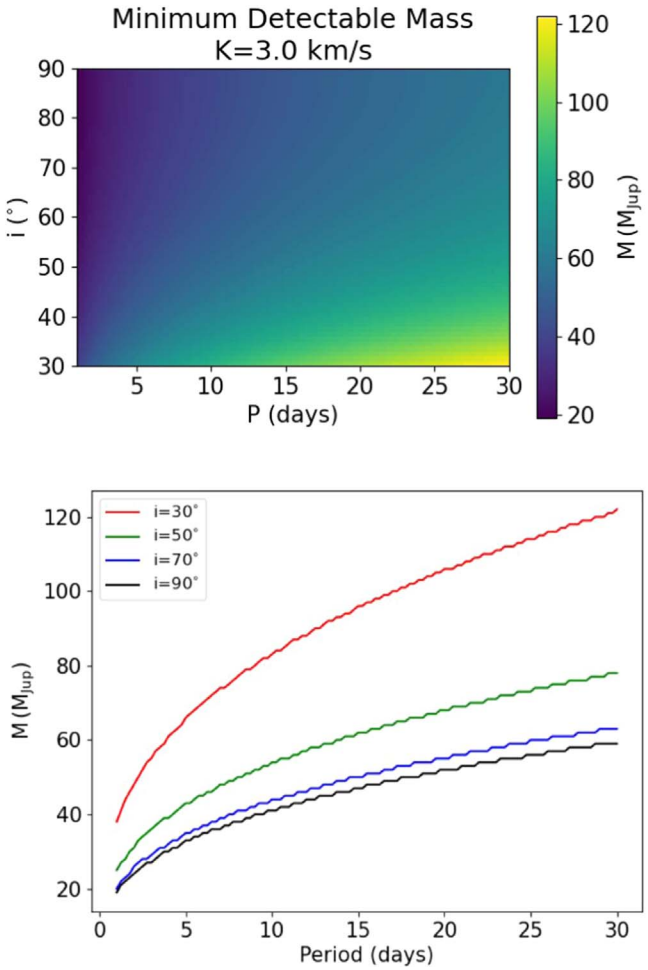

Figure 3. (Top) Minimum detectable binary companion mass for various periods (P) and inclinations (i). For a given combination of period and inclination, the reported "minimum detectable mass" can be found, which corresponds to the lowest mass a companion would have that would result in a semiamplitude $K > 3$ km s^{-1}. Any companions less than that mass would be undetectable in the spectroscopic data and any companions that were more massive would have been detected. (Bottom) Minimum detectable mass as a function of period for selected inclinations.

not consistent with oscillatory behavior caused by a close-in companion.

Both sets of measurements are consistent with constant values to within one standard deviation, except for a single point: the radial velocity measured from the second spectrum on BJD 2459608. In both cases we see that we would be sensitive to any periodic signal with a semiamplitude $K \gtrsim 3$ km s^{-1}, while any signal that has $K \lesssim 3$ km s^{-1} may still be hidden within the measurement error.

Using Equation (1)—which relates the semiamplitude K to the orbital period P of a companion of mass M_2 around a host of mass M_1 with eccentricity and inclination e and i—it is possible to estimate the detectable companion mass for a given set of P, i, and e values.

$$K = \left(\frac{2\pi G}{P}\right)^{1/3} \frac{M_2 \sin(i)}{(M_2 + M_1)^{2/3}} \frac{1}{\sqrt{1 - e^2}}. \quad (1)$$

For this estimation $K_{\max} = 3$ km s^{-1} and e is assumed to be equal to 0. We then vary P and i and calculate the smallest mass that would generate an RV semiamplitude $K > K_{\max}$ for each (P, i) combination. The results of this are shown in Figure 3 for $2 \leqslant P \leqslant 30$ days and $30° \leqslant i \leqslant 90°$.

The choice to restrict this analysis to periods between 2 and 30 days is due to the cadence of observations and the duration of the survey. A companion with a shorter period may still have been detectable although without being able to accurately measure the period. We would not have enough data to detect a companion with a period $P \gtrsim 30$ days since there would be insufficient time to see periodicity in the signal; however, our data do cover the range of expected periods for an RS CVn system ($P \lesssim 14$ days). With regards to the inclination the analysis is not performed below 30° due to the difficulty of detecting companions in RV signals for near face on orbits. The original claim was of this star as a spectroscopic binary, meaning that the system would not have been face on.

At the extreme values of the analysis we find that a binary companion with $P = 2$ days and $i = 90°$ would be detectable if it had a mass greater than 24 M_J whereas for a companion with $P = 30$ days and $i = 30°$ the minimum mass that would be detectable via an RV signal would be 122 M_J. This tells us that in the spectroscopic data taken on this star we would have seen the signature for a binary companion above 122 M_J at worst and 24 M_J at best.

Further spectroscopic data taken at higher precision and over longer times will aid in ruling out potential lower-mass and longer-period binary companions, but current data suggest there is no companion with mass greater than 122 M_J with a duration less than 30 days, which is sufficient to refute previous evidence of this star being a spectroscopic binary.

3.2. Nondetection of Ca HK Emission

We also reassess evidence that HIP 5319 has a high chromospheric activity. Boro Saikia et al. (2018) previously

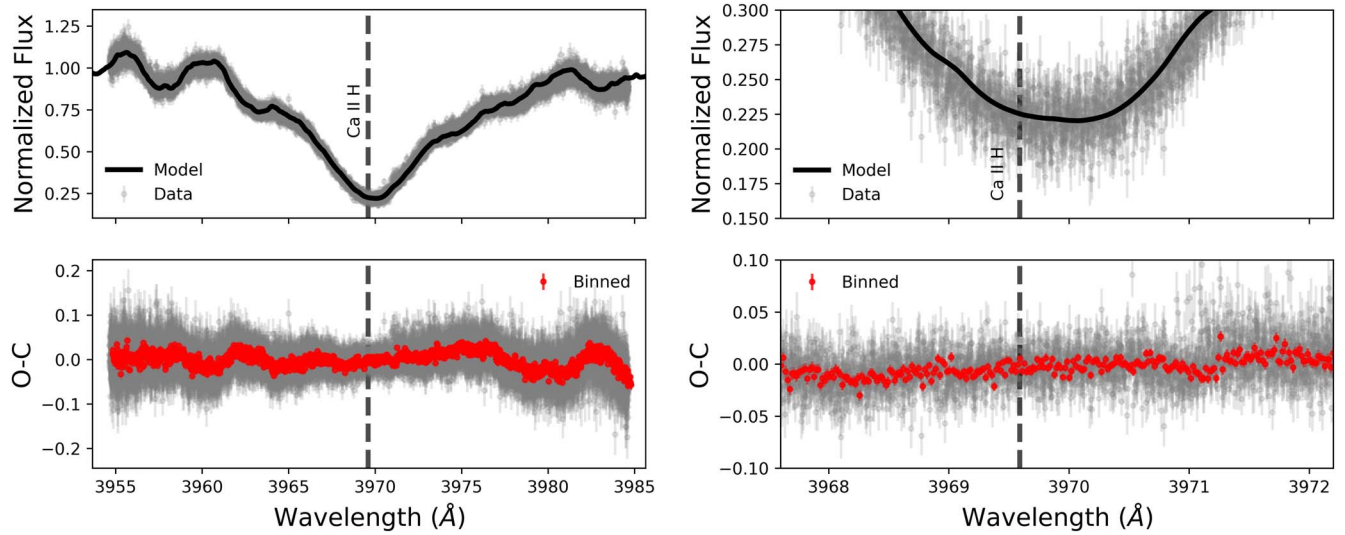

Figure 4. Data from LCOGT NRES spectra of the primary star HIP 5319 A compared to a PHOENIX model spectrum for an F5IV star surrounding the Ca II H line at its vacuum wavelength $\lambda = 3969.5$ Å. The model spectrum has been broadened by 100 km s^{-1} to match the best-fit $v\sin(i)$ value for the Ca II H line from the LCOGT spectra. (Left top) Model spectra plotted over data from the 12 LCOGT spectra between $\lambda = 3955$–3985 Å. (Left bottom) The O−C (Observed−Calculated) plot showing the residuals between measured data and model. Gray points are the residuals from each of the 12 spectra, while the red points are rebinned to the original NRES spectral resolution. (Right) The same data and residuals between $\lambda = 3968$–3972 Å. In both cases it can be clearly seen that there is no excess flux beyond the 1% level in the spectrum at any point near the Ca H line.

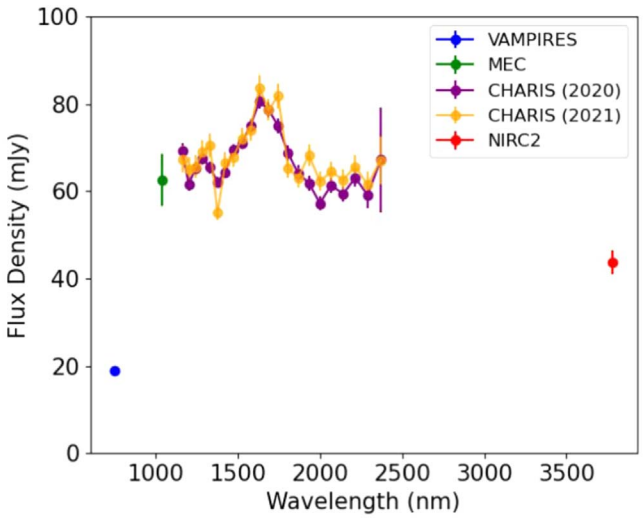

Figure 5. Combined SCExAO/CHARIS spectra, SCExAO/MEC photometry, SCExAO/VAMPIRES and Keck/NIRC2 photometry of the low-mass companion HIP 5319 B taken on 2020 July 31 (CHARIS and MEC), 2021 September 11 (CHARIS and VAMPIRES), and 2022 January 15 (NIRC2) at the Subaru and Keck II telescopes. The reddest CHARIS channel has substantially higher uncertainty in our spectrophotometric calibration because we did not obtain sky frames.

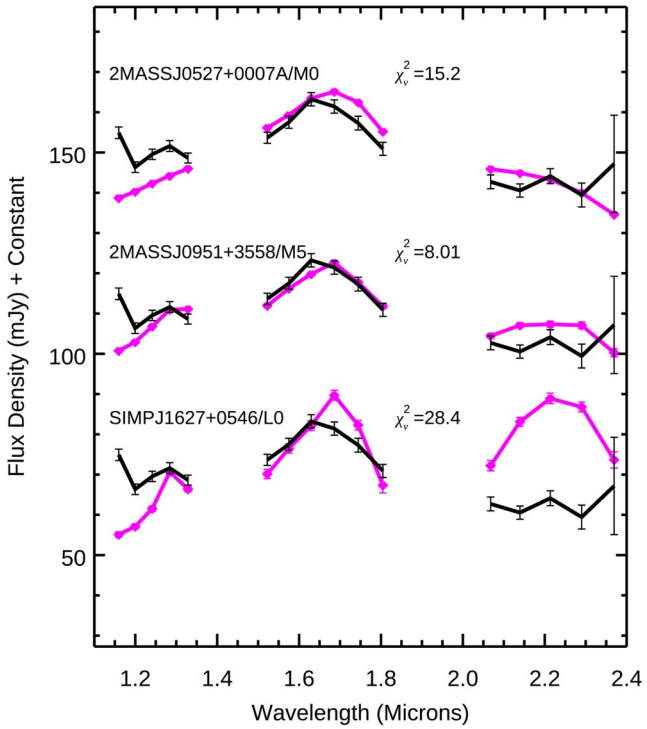

Figure 6. The CHARIS HIP 5319 B spectrum (black) compared to those of field brown dwarfs (magenta) with spectral types M0, M5, and L0 from the Montreal Spectral Library binned to CHARIS's resolution.

claim to have measured a value of $\log(R'_{HK}) = -4.016$. The methodology behind this claim was to measure the surface flux R_{HK} by coadding all available spectra for the target into a template spectra that was then normalized to a PHOENIX model atmosphere in order to convert to absolute flux units. The photospheric flux contribution $R_{\rm phot} = F_{\rm phot}/\sigma T_{\rm eff}^4$ was then subtracted from the integrated flux of the Ca II H and K line cores from the PHOENIX model atmosphere. The excess that was seen after this subtraction interpreted as being from emission at the H and K lines.

By comparing the high-resolution LCOGT spectra (Section 2.2.5, Table 2) and the model PHOENIX spectrum for an F5IV star used for photometric calibration (Sections 2.2.2, 2.2.3), we find no evidence to support the claim of any excess flux around the Ca II H or K lines beyond the 1% level.

To compare the difference between the model PHOENIX spectrum and LCOGT spectra, each nightly spectrum was individually normalized using a scale factor, slope, and offset. Figure 4 shows the result of this comparison for the Ca II H line at $\lambda = 3969.5$ Å.

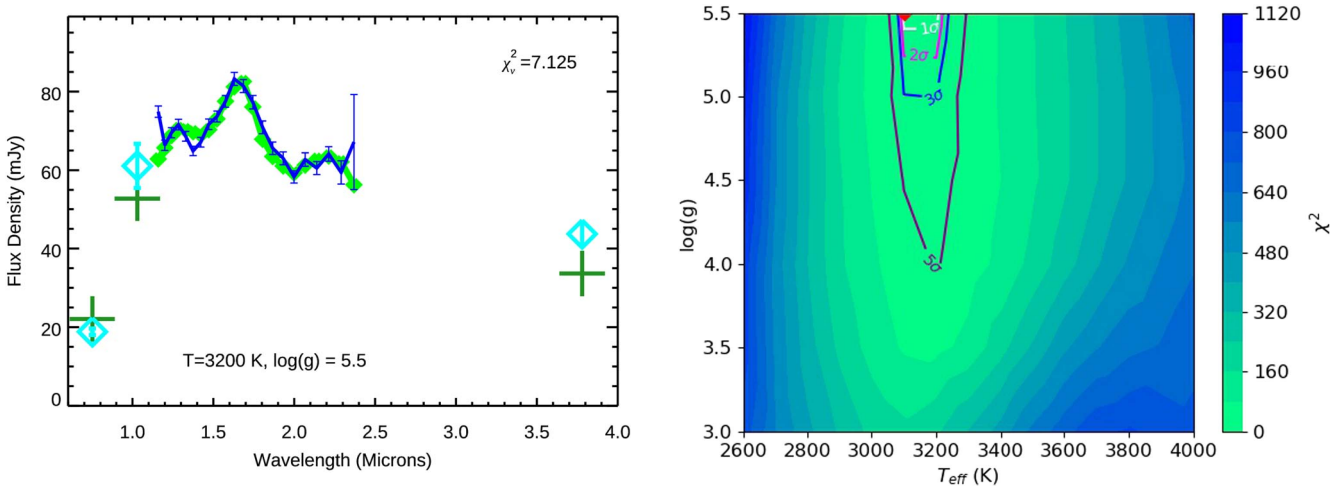

Figure 7. (Left) BT-Settl model for solar metallicity with $T = 3200$ K and $\log(g) = 5.5$. CHARIS spectra is shown in dark blue, VAMPIRES, MEC, and NIRC2 photometry in cyan compared to the model-predicted CHARIS spectrophotometry in light green, and predicted VAMPIRES/MEC/NIRC2 photometry (dark green crosses). Although the S/N of the spectrum is quite high, the spectral covariance in the CHARIS data is also high, leading to a large value of χ^2. (Right) Corresponding contour plots for χ^2 as a function of temperature and surface gravity. The best-fit solution is shown with a red diamond while the 1σ, 2σ, 3σ, and 5σ contours are shown in white, magenta, blue, and purple, respectively.

The top panels in Figure 4 show the data from all of the spectra in Table 2 compared to the model PHOENIX spectrum, while the bottom panels show the residuals between the data and model. The residuals from each spectra compared to the model are shown as gray points, while the red points show the residuals when the data are rebinned to the original NRES $R \sim 50{,}000$. This rebinning was performed because each spectra that makes up the combined data set (made of 12 individual spectra) samples slightly different rest-frame wavelengths because of the evolving barycenter velocity over the 23 days where spectra were collected. This means that there is roughly 12 times as much data since the same wavelengths are not sampled multiple times. By rebinning to the original NRES resolution this has the effect of demonstrating what a single spectra would look like for ~12 times as much observation time as one of the individual spectra on its own.

The data collected in the 14 observations match the model without any significant deviation around the cores of the Ca II HK lines. Along with the nondetection of an time-varying signal in the RV and $v\sin(i)$ data this refutes the evidence that the primary is an RS CVn binary which is expected to have high chromospheric activity and a period below 14 days, meaning it is likely a single star. This is in good agreement with the report of HIP 5319A from the Gaia Early Data Release 3 (Gaia eDR3; Brown et al. 2021) as being well fit by a five-parameter single-star solution whose renormalized unit weight error is 1.01, which effectively rules out stellar-mass companions greater than ~0.4 $M_\odot$ and a period between 1 and 10 days.

3.3. Spectrum of HIP 5319 B

Figure 5 shows the 2020 and 2021 CHARIS spectra (whose data can be found in Table 4) as well as MEC,[25] VAMPIRES, and NIRC2 photometric points. The MEC photometry and CHARIS spectra are flat in F_ν units except for a broad peak in H band. Formally, the S/N of HIP 5319 B in each spectral channel is extremely high (S/N > 77). Outside of the H band, peak, consecutive wavelength channels show a "wavy" pattern, which may indicate the impact of spectrally correlated noise (see below). The two CHARIS spectra show broad agreement: due to the higher S/N for the 2020 epoch spectrum, we focus on it for subsequent analysis.

HIP 5319 B's broadband near-IR colors ($J–H \sim 0.57 \pm 0.03$; $H–K_s \sim 0.24 \pm 0.03$) resemble those of early-to-mid M dwarfs (Pecaut & Mamajek 2013). HIP 5319 B is substantially fainter than the primary in the VAMPIRES 750 nm data ($\Delta m \sim 7.110$). The VAMPIRES filter does not correspond to any standard photometric bandpass with a published zero-point flux density but lies between the Johnson-Cousins R and I bands. Adopting again the standard colors from Pecaut & Mamajek (2013) and R-band optical photometry for the primary from the *Simbad* database, we estimate a pseudomagnitude of ≈13 at 750 nm.

We compare HIP 5319 B's CHARIS spectrum with other low-mass objects in the Montreal Spectral Library[26] (e.g., Gagné et al. 2015). Only the CHARIS spectrum was used because the wavelength range for the Montreal Spectral Library covers *JHK*, but is rather nonuniform otherwise. Following the methods described in Greco & Brandt (2016), we find that the CHARIS spectrum shows noise that is high spatially and spectrally correlated ($A_\rho \sim 0.69$, $A_\lambda \sim 0.22$). HIP 5319 B is best matched by an M3–M7 dwarf: earlier M dwarfs and L dwarfs fail to reproduce the CHARIS spectra, especially in the J and K bands (see Figure 6).

Following similar analysis in Steiger et al. (2021), we compared the MEC, VAMPIRES, and NIRC2 photometry, and CHARIS spectrum to the BT-Settl atmosphere models (Allard et al. 2012) with the Asplund et al. (2009) abundances and solar metallicities. We focus only on the CHARIS channels unaffected by telluric absorption and also remove the first CHARIS channel, whose high flux density is not reproduced in any empirical spectrum in the Montreal Library. We define the fit quality for the kth model using the χ^2 statistic, considering the spectral covariance.

[25] Although the MEC data has a median spectral resolution $\mathcal{R} \sim 4.0$, we bin our spectral data to a single Y-band photometry point for comparison with the standard photometric band.

[26] https://jgagneastro.com/the-montreal-spectral-library/

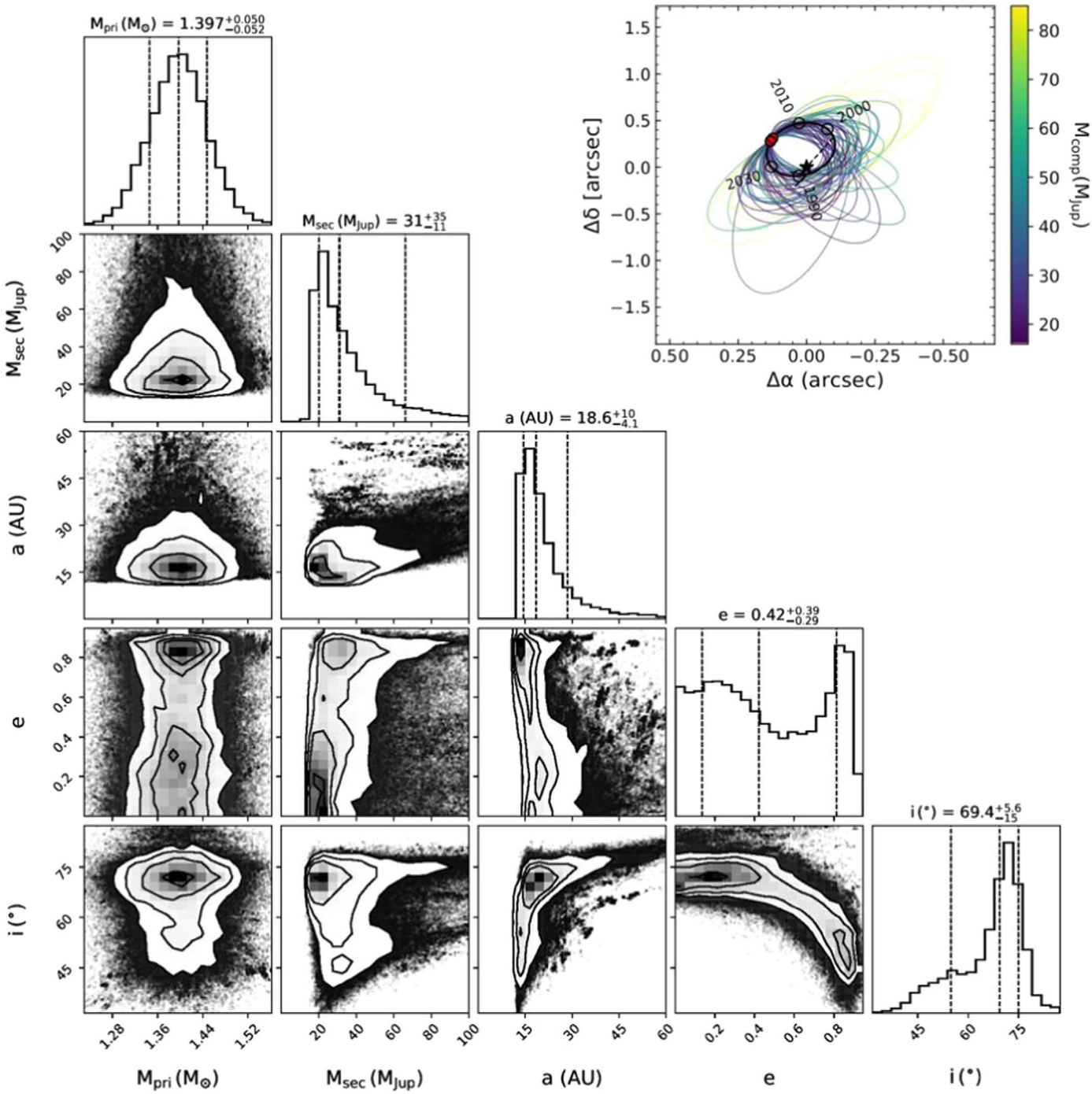

Figure 8. Corner plot showing the posterior distributions of selected orbital parameters using a log-normal (1/M) prior for the mass of the secondary companion. The orbit fits used Hipparcos and Gaia (HGCA) absolute astrometry and relative astrometry from SCExAO/CHARIS and MEC data. The inset in the figure shows the best-fit orbit (black) with 50 random orbits drawn from the MCMC fits color coded by the mass of HIP 5319 B. The red-colored points in the orbit represent relative astrometry points from the three epochs where data were taken, and the unfilled circles show the predicted location of the companion at different past and future epochs. The companion is orbiting counterclockwise.

Figure 7 shows the best-fit solar metallicity model and associated χ^2 contours. An atmosphere with a temperature of $T_{\rm eff}$ = 3100–3200 K and a high gravity ($\log(g) = 5.5$) fits the data the best,[27] although the family of solutions drawn from high gravity models ($\log(g)$ = 5–5.5) at 3100 K and 3300 K, and those at 3200 K and a lower gravity of $\log(g)$ = 4–4.5 fall within 5$\sigma$of the best-fit model. The radii that minimize χ^2 are 3.25–3.62 $R_{\rm J}$, yielding a luminosity of $\log(L/L_{\odot}) = -1.94 \pm 0.04$. The best-fitting atmospheric models ($\log(g) = 5.5$, $R_{\rm sec}$ = 3.4–3.59 R_J) correspond to a companion whose mass is ∼448–1675 $M_{\rm Jup}$, or 0.427–1.60 $M_{\odot}$. Some of these values would be significantly higher than those for a typical M3-M7 star (Pecaut & Mamajek 2013), potentially greater than the mass of the primary itself. However, 5σ confidence interval containing lower gravity solutions implies masses down to 44 $M_{\rm J}$ and includes a wider range of radii (3.25–3.62 $R_{\rm J}$). Thus,

[27] Fits at 3100 *K* and 3200 *K* are almost numerically equivalent.

Table 4
HIP 5319 B Spectra

	2020 July 31			2021 September 11		
Wavelength (μm)	F_ν (mJy)	σF_ν (mJy)	S/N	F_ν (mJy)	σF_ν (mJy)	S/N
1.160	69.197	1.720	61.8	67.313	3.076	52.7
1.200	61.625	1.612	56.7	65.107	2.733	55.5
1.241	65.347	1.490	72.5	65.612	2.589	55.9
1.284	67.608	1.490	84.7	68.917	2.856	47.0
1.329	65.402	1.407	82.0	70.522	2.650	58.4
1.375	62.158	1.237	111.0	55.005	1.672	78.1
1.422	64.376	1.308	106.7	66.510	2.453	77.4
1.471	69.387	1.408	118.3	67.856	2.367	93.6
1.522	71.086	1.419	141.1	71.960	2.449	85.6
1.575	74.866	1.518	150.9	74.057	2.521	71.3
1.630	80.553	1.703	130.8	83.695	2.936	76.6
1.686	78.667	1.716	116.0	78.616	2.461	81.6
1.744	74.888	1.802	101.4	81.785	2.802	78.7
1.805	68.638	1.745	83.4	65.169	2.220	66.7
1.867	64.104	1.793	67.1	63.105	2.272	74.0
1.932	61.858	1.793	71.5	68.272	2.493	117.6
1.999	57.205	1.672	77.4	62.256	2.167	94.3
2.068	61.378	1.770	102.2	64.435	2.329	89.4
2.139	59.341	1.688	109.1	62.607	2.294	87.4
2.213	63.070	1.926	93.5	65.636	2.625	83.0
2.290	59.136	3.066	64.8	61.504	2.955	87.8
2.369	67.170	12.091	68.5	67.050	5.416	53.3

Note. Throughput-corrected HIP 5319 B spectra extracted from 2020 July and 2021 September CHARIS data.

while the temperature of HIP 5319 B is well constrained to 3100–3300 *K*, the companion's poorly constrained surface gravity results in poor mass limits.

Using isochrones from Baraffe et al. (2015) we find that using the age estimate of 1.07–1.23 Gyr from the Padova and BASTI models in (Casagrande et al. 2011) and adopting the luminosity of $\log(L/L_\odot = -1.94 \pm 0.04)$ from the atmospheric models we estimate the mass of the secondary would fall between roughly 0.3–0.35 $M_\odot$. Considering the *widest* possible range of ages of 8 Myr to 2 Gyr (the lowest end predicted by Stanford-Moore et al. 2020 and the highest predicted by Holmberg et al. 2009) we find that the range of masses extends from $40 M_{\rm Jup}$ to 0.35 $M_\odot$. Both possible ranges include typical masses of M dwarfs from Pecaut & Mamajek (2013), while the low end of the range suggest masses down to $40 M_{\rm Jup}$, which does not disagree with either the dynamical mass (see Section 3.4) or the mass estimated from the atmospheric models above.

3.4. Orbit and Dynamical Mass

We used the open-source code `orvara` (Brandt et al. 2021) to fit for the mass and orbit of HIP 5319 B. `orvara` uses a combination of radial-velocity (RV) absolute astrometry of the primary, and relative astrometry of the low-mass companion to measure orbital parameters even when the observations of the companion only cover small fractions of an orbit.

3.4.1. Results Using a $1/M_p$ Prior for Companion Mass

For this companion, we used HGCA absolute astrometry measurements for the star and three epochs of relative astrometry from CHARIS, MEC, and NIRC2. There is no archival RV data for this target and so it is not included in the `orvara` fits. A Gaussian prior of $1.4 \pm 0.05\, M_\odot$ was chosen based on literature values for the primary mass (Casagrande et al. 2011), while a log-flat (1/M) prior was chosen for the mass of HIP 5319 B, which is the default used by `orvara`. This choice is motivated by the shape of the initial mass function for low-mass objects and for planets, which says that low-mass objects are expected to occur more frequently than high-mass ones (Chabrier 2003; Nielsen et al. 2019).

Figure 8 shows the posterior distributions for the primary and secondary masses along with select orbital parameters. The fit parameters are also summarized in Table 5. The primary mass of $1.397^{+0.050}_{-0.052} M_\odot$ is nearly the same as the adopted prior and the secondary mass best-fit value is $31^{+35}_{-11} M_{\rm Jup}$. The companion has a best-fit semimajor axis of $18.6^{+10}_{-4.1}$ au with an eccentricity of $0.42^{+0.39}_{-0.29}$ and inclination of $69.4^{+5.6}_{-15}$ degrees.

From the corner plot and inset in Figure 8, it is clear that the low-mass solutions favor less eccentric orbits at shorter semimajor axes. We also note the bimodal behavior of the distribution of eccentricities with peaks at $e \sim 0.13$ and ~ 0.81. Continued monitoring in follow-up observations will serve to further constrain the best-fit values for the orbit of this companion as greater fractions of its orbit are observed.

3.4.2. Results Using a Gaussian Prior for Companion Mass

We have focused on the `orvara` fits using a log-flat prior for the secondary mass. However, the mass function near the hydrogen-burning limit exhibits a turnover, where lower-mass objects are less common (Chabrier 2003). To investigate how the choice of prior may affect the posterior distribution for companion mass, we reran `orvara` using a Gaussian prior of $M_{\rm sec} = 0.2 \pm 0.1 M_\odot$ ($210 \pm 105 M_{\rm Jup}$), comparable to the implied masses for M3–M7 stars (Section 3.3). It is also similar to the turnover in the binary mass function from Chabrier (2003). Assuming this companion is on the main sequence, the upper limit of its mass

Table 5
HIP 5319 B Orbit-fitting Results and Priors

Parameter	Fitted Value	Prior
$M_{\rm pri}$ ($M_\odot$)	$1.397^{+0.050}_{-0.052}$	Gaussian, 1.4 ± 0.05
$M_{\rm sec}$ ($M_{\rm Jup}$)	31^{+35}_{-11}	$1/M_{\rm sec}$ (log flat)
Semimajor axis a (au)	$18.6^{+10}_{-4.1}$	$1/a$ (log flat)
Eccentricity e	$0.42^{+0.39}_{-0.29}$	uniform
Inclination i (°)	$69.4^{+5.6}_{-15}$	sin i (geometric)

Note. Posterior distributions for the secondary mass and semimajor axis are both positively skewed and favor low-mass, low-separation distributions. The eccentricity is not well constrained using only two relative astrometry points and no RV data, though future astrometry for this target should serve to better constrain this value.

Table 6
HIP 5319 B Orbit-fitting Results For Different Priors on Secondary Mass

Parameter	log-flat (1/M)	Gaussian ($0.2 \pm 0.1 M_\odot$)
$M_{\rm pri}$ ($M_\odot$)	$1.397^{+0.050}_{-0.052}$	$1.399^{+0.051}_{-0.050}$
$M_{\rm sec}$ ($M_{\rm Jup}$)	31^{+35}_{-11}	128^{+127}_{-88}
Semimajor axis a (au)	$18.6^{+10}_{-4.1}$	36^{+17}_{-17}
Eccentricity e	$0.42^{+0.39}_{-0.29}$	$0.33^{+0.38}_{-0.24}$
Inclination i (°)	$69.4^{+5.6}_{-15}$	$75.5^{+3.9}_{-9.0}$

Note. Posterior distributions for two different priors on the secondary mass. The priors on all other parameters being fit remain unchanged between the simulations and can be found for reference in Table 5.

would be $M_{\rm sec} \sim 0.3$–$0.4\ M_\odot$. This prior therefore encompasses these potential values by creating a Gaussian where the expected values of the secondary mass will fall between $+2\sigma$ and -2σ.

Table 6 lists the resulting best-fit posterior values; Figure 9 displays the corner plot showing the posterior distributions. The eccentricity and inclination distributions —$e = 0.33^{+0.38}_{-0.24}$, $i = 75^{+3.9}_{-9.0}$ degrees—agree with earlier analyses. However, compared to results for a log-normal companion mass prior, the median of the posterior distributions for HIP 5319 B's mass and semimajor axis have shifted to larger values: $128^{+127}_{-88}\ M_{\rm Jup}$ and 36^{+17}_{-17} au. For companion mass, the posterior distribution peak is $\sim$20–40 $M_{\rm J}$, comparable to values derived assuming a log-normal companion mass prior. But the posterior distribution includes a tail of far higher mass solutions, out to $\sim$350 $M_{\rm J}$, resulting in a far larger median value. The semimajor axis posterior distribution contains two peaks—one near 18 au and a second near 35–40 au.

In practical terms, our analyses are unable to conclusively clarify whether HIP 5319 B is a brown dwarf or a low-mass star. Dynamical modeling assuming a log-normal companion mass prior favors a brown dwarf at 18.6 au, while modeling adopting a Gaussian prior admits a much wider range of companion masses, including those on both sides of the hydrogen-burning limit. The implied masses from masses from atmospheric modeling admit a wide range of possible values: 44 $M_{\rm J}$ to 1675 $M_{\rm J}$. However, the orbit insets to Figures 8 and 9 suggest that future astrometric monitoring of HIP 5319 B should clarify the companion's nature.

4. Summary and Discussion

SCExAO/CHARIS spectroscopy and photometry from SCExAO/MEC, SCExAO/VAMPIRES, and Keck/NIRC2 have enabled the identification of a candidate substellar companion to the young F5IV star HIP 5319. Comparisons of the SCExAO/CHARIS spectra to the spectra of objects in the Montreal Spectral Library show this companion to be best matched with M3-M7 dwarfs, with earlier-type M and L dwarfs failing to match the CHARIS spectra measured in J and K bands. By combining measurements from Hipparcos and Gaia with our relative astrometry from CHARIS/MEC/VAMPIRES/NIRC2 we can constrain the dynamical mass and orbit of HIP 5319 B.

Assuming a log-normal prior, we find a dynamical mass of $31^{+35}_{-11} M_{\rm Jup}$ for the companion, suggesting that HIP 5319 B is a brown dwarf. The posterior distributions from the fits for dynamical mass show a bimodal distribution in possible eccentricity values, where high-eccentricity solutions are favored at more edge-on inclinations and low-eccentricity solutions are favored for more inclined orbits. However, adopting a Gaussian prior for the companion mass yields a higher mass of $128^{+127}_{-88} M_{\rm J}$, which favors the interpretation of the companion as a low-mass star although the distribution's peak still falls in the substellar range. Future RV measurements, relative astrometry from direct imaging instruments and more precise astrometry from Gaia data releases will contribute to further constraining this companion's mass and orbital parameters, providing deeper clarity on this companion's identity.

Atmospheric models of the companion show a best fit to an atmosphere with solar metallicity at $T = 3200$ K with a surface gravity $\log(g) = 5.5$, though solutions with comparably good fits exist with temperatures that range from 3100 to 3300 K and slightly lower surface gravities ($\log(g) = 4$–4.5). The best-fit models show radii between 3.25 and 3.62 R_J and $\log(L/L_\odot) = -1.94 \pm 0.04$. The mass inferred from atmospheric modeling is poorly constrained.

This work highlights the need to have an updated inventory of system measurements when interpreting companions imaged around accelerating stars. While much older data suggested that HIP 5319 is a RS CVn (short-period) binary, our RV data rule out stellar companions with an orbital period less than 30 days whose presence would affect our conclusions about HIP 5319 B's mass and orbital properties. Similarly, our HIP 5319 spectra find no evidence for Ca HK emission that could reveal evidence of HIP 5319's youth. Other system measurements whose values may impact derived companion masses and orbits include spectral type/luminosity, projected rotation rate, lithium abundances, x-ray activity, etc.

Finally, this work demonstrates the importance of priors in dynamical models used to estimate companion masses and orbits from direct imaging and astrometry. When a small fraction of a companion's orbit has been observed—as is the case with HIP 5319 B—the selection of prior for a given parameter may influence the final shape of the posterior distributions and the reported values of the dynamical mass and orbital parameters. The chosen prior should not cause the fitted values to change significantly (see also Currie et al. 2022b). Performing multiple fits for orbital parameters using disparate priors (e.g., Gaussian, log-normal, uniform, geometric, depending on the parameter of interest) can confirm that the extracted masses and orbital parameters are robust. If the results from multiple fits are in good agreement with one another—the values within the 95% or 68% confidence interval overlap with one another, for example—one may say conclusively that the

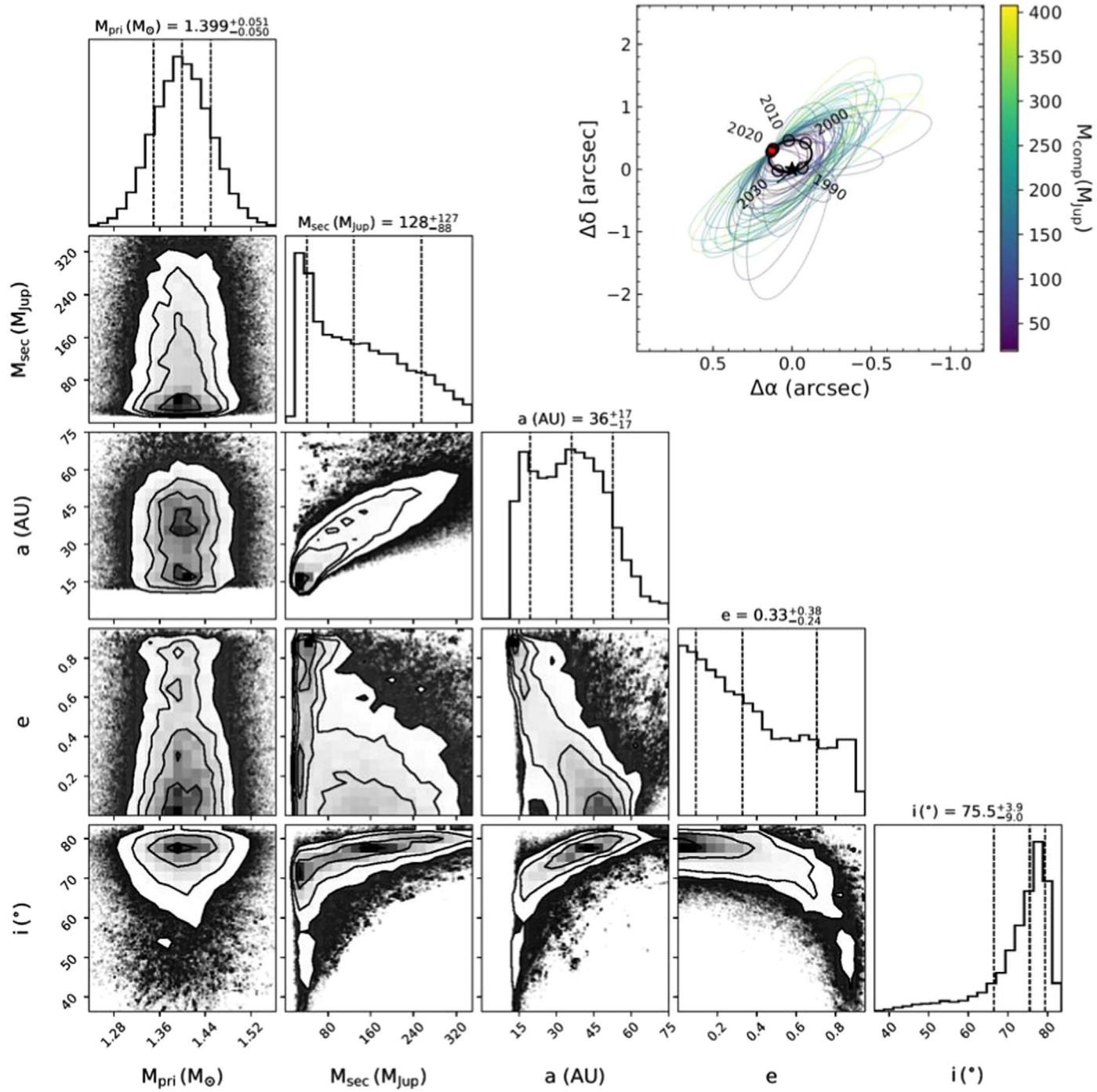

Figure 9. Corner plot showing the posterior distributions of selected orbital parameters using a Gaussian prior of $0.2 \pm 0.1 M_\odot$ for the mass of the secondary companion. The orbit fits used Hipparcos and Gaia (HGCA) absolute astrometry and relative astrometry from SCExAO/CHARIS and MEC data. The inset in the figure shows the best fit orbit (black) with 50 random orbits drawn from the MCMC fits color coded by the mass of HIP 5319 B. The red-colored points in the orbit represent relative astrometry points from the three epochs where data were taken, and the unfilled circles show the predicted location of the companion at different past and future epochs. The companion is orbiting counterclockwise.

derived dynamical mass is robust. Otherwise, the data are not sufficiently constraining: more of the orbit must then be observed before one can make a definitive claim regarding the fitted orbital parameters and masses of the system.

This direct imaging detection was—in part—made due to the identification of the system as having statistically significant astrometric acceleration in the HGCA. Previous works, which include—but are not limited to—Brandt et al. (2019), Kervella et al. (2019), Currie et al. (2020), Bonavita et al. (2020), Bowler et al. (2021), Chilcote et al. (2021), Li et al. (2021), Steiger et al. (2021), Currie et al. (2022b), Kuzuhara et al. (2022), Miskovetz et al. (2022), and Salama et al. (2022), have also used the HGCA to select targets that have been found to host previously unidentified companions. This discovery further demonstrates the efficacy of using astrometry to select direct imaging targets instead of conducting blind searches. As more HGCA targets are observed, future Gaia data releases yield more precise astrometry, and direct imaging capabilities

improve, this survey approach will only become more powerful in discovering substellar companions, including numerous planets (Currie et al. 2021).

The authors wish to recognize and acknowledge the very significant cultural role and reverence that the summit of Maunakea has always had within the indigenous Hawaiian community. We are most fortunate to have the opportunity to conduct observations from this mountain.

We also wish to thank Eric Mamajek, Jonathan Gagne, and Kris Hełminiak for their helpful comments about the HIP 5319 system properties. We thank the Las Cumbres Observatory for their approval of director's discretionary time (DDT) in order to perform spectroscopic follow-up of the primary under project code DDT2021B-007.

The development of SCExAO was supported by the Japan Society for the Promotion of Science (Grant-in-Aid for Research #23340051, #26220704, #23103002, #19H00703, and #19H00695), the Astrobiology Center of the National Institutes of Natural Sciences, Japan, the National Astronomical Observatory of Japan, and the Mt Cuba Foundation.

T.C. was supported by a NASA Senior Postdoctoral Fellowship and NASA/Keck grant LK-2663-948181. T.B. gratefully acknowledges support from the Heising-Simons foundation and from NASA under grant #80NSSC18K0439. M.T. is supported by JSPS KAKENHI grant # 18H05442. N.Sk. and V.D. acknowledge support from NASA (grant #80NSSC19K0336). S.S. is supported by a grant from the Heising-Simons Foundation. N.Z. was supported throughout this work by a NASA Space Technology Research Fellowship. K.K.D. is supported by an NSF Astronomy and Astrophysics Postdoctoral Fellowship under award AST-1801983.

Facilities: Subaru/SCExAO, Keck/NIRC2, Las Cumbres Observatory Global Telescopes (LCOGT).

Software: MKID Data Reduction Pipeline (Walter et al. 2020, Steiger et al. 2022), `orvara` (Brandt et al. 2021), CHARIS Data Reduction Pipeline (Brandt et al. 2017), CHARIS Data Processing Pipeline (Currie et al. 2020), `matplotlib`, `astropy`, BANZAI-NRES.

ORCID iDs

Noah Swimmer https://orcid.org/0000-0001-5721-8973
Thayne Currie https://orcid.org/0000-0002-7405-3119
Sarah Steiger https://orcid.org/0000-0002-4787-3285
G. Mirek Brandt https://orcid.org/0000-0003-0168-3010
Timothy D. Brandt https://orcid.org/0000-0003-2630-8073
Olivier Guyon https://orcid.org/0000-0002-1097-9908
Masayuki Kuzuhara https://orcid.org/0000-0002-4677-9182
Tyler D. Groff https://orcid.org/0000-0001-5978-3247
Julien Lozi https://orcid.org/0000-0002-3047-1845
John I. III Bailey https://orcid.org/0000-0002-4272-263X
Nicholas Zobrist https://orcid.org/0000-0003-3146-7263
Jennifer Pearl Smith https://orcid.org/0000-0002-0849-5867
Kristina K. Davis https://orcid.org/0000-0001-5587-845X
Sebastien Vievard https://orcid.org/0000-0003-4018-2569
Nour Skaf https://orcid.org/0000-0002-9372-5056
Vincent Deo https://orcid.org/0000-0003-4514-7906
Nemanja Jovanovic https://orcid.org/0000-0001-5213-6207
Frantz Martinache https://orcid.org/0000-0003-1180-4138
Motohide Tamura https://orcid.org/0000-0002-6510-0681
Benjamin A. Mazin https://orcid.org/0000-0003-0526-1114

References

Ahn, K., Guyon, O., Lozi, J., et al. 2021, Proc. SPIE, 11823, 9
Allard, F., Homeier, D., & Freytag, B. 2012, RSPTA, 370, 2765
Asplund, M., Grevesse, N., Sauval, A. J., & Scott, P. 2009, ARA&A, 47, 481
Baraffe, I., Homeier, D., Allard, F., & Chabrier, G. 2015, A&A, 577, A42
Blanco, C., Bruca, L., Catalano, S., & Marilli, E. 1982, A&A, 115, 280
Blunt, S., Wang, J. J., Angelo, I., et al. 2020, AJ, 159, 89
Bonavita, M., Fontanive, C., Desidera, S., et al. 2020, MNRAS, 494, 3481
Bonavita, M., Fontanive, C., Gratton, R., et al. 2022, MNRAS, 513, 5588
Boro Saikia, S., Marvin, C. J., Jeffers, S. V., et al. 2018, A&A, 616, A108
Bowler, B. P., Cochran, W. D., Endl, M., et al. 2021, AJ, 161, 106
Brandt, G. M., Dupuy, T. J., Li, Y., et al. 2021, AJ, 162, 301
Brandt, T. D. 2021, ApJS, 254, 42
Brandt, T. D., Dupuy, T. J., & Bowler, B. P. 2019, AJ, 158, 140
Brandt, T. D., Dupuy, T. J., Li, Y., et al. 2021, AJ, 162, 186
Brandt, T. D., Rizzo, M., Groff, T., et al. 2017, JATIS, 3, 048002
Brown, A. G. A., Vallenari, A., Prusti, T., et al. 2018, A&A, 616, A1
Brown, A. G. A., Vallenari, A., Prusti, T., et al. 2021, A&A, 650, C3
Brown, T. M., Baliber, N., Bianco, F. B., et al. 2013, PASP, 125, 1031
Carson, J., Thalmann, C., Janson, M., et al. 2013, ApJL, 763, L32
Casagrande, L., Schönrich, R., Asplund, M., et al. 2011, A&A, 530, A138
Chabrier, G. 2003, ApJL, 586, L133
Chauvin, G., Desidera, S., Lagrange, A. M., et al. 2017, A&A, 605, L9
Cheetham, A., Bonnefoy, M., Desidera, S., et al. 2018, A&A, 615, A160
Chilcote, J., Tobin, T., Currie, T., et al. 2021, AJ, 162, 251
Currie, T., Biller, B., Lagrange, A.-M., et al. 2022a, arXiv:2205.05696
Currie, T., Brandt, G. M., & Brandt, T. D. 2022b, submitted
Currie, T., Cloutier, R., Brittain, S., et al. 2015, ApJL, 814, L27
Currie, T., Daemgen, S., Debes, J., et al. 2014, ApJL, 780, L30
Currie, T., Burrows, A., Itoh, Y., et al. 2011, ApJ, 729, 128
Currie, T., Debes, J., Rodigas, T. J., et al. 2012, ApJL, 760, L32
Currie, T., Brandt, T. D., Uyama, T., et al. 2018a, AJ, 156, 291
Currie, T., Kasdin, N., Groff, T., et al. 2018b, PASP, 130, 044505
Currie, T., Marois, C., Cieza, L., et al. 2019, ApJL, 877, L3
Currie, T., Brandt, T. D., Kuzuhara, M., et al. 2020, ApJL, 904, L25
Currie, T., Guyon, O., Lozi, J., et al. 2020, Proc. SPIE, 11448, 114487H
Currie, T., Brandt, T. D., Kuzuhara, M., et al. 2021, Proc. SPIE, 11823, 22
Currie, T., Lawson, K., Schneider, G., et al. 2022c, NatAs, 6, 751
Danziger, I. J., & Faber, S. M. 1972, A&A, 18, 428
de Medeiros, J. R., & Mayor, M. 1999, A&AS, 139, 433
Desidera, S., Chauvin, G., Bonavita, M., et al. 2021, A&A, 651, A70
Favata, F., Micela, G., & Sciortino, S. 1995, A&A, 298, 482
Fleming, T. A., Gioia, I. M., & Maccacaro, T. 1989, ApJ, 340, 1011
Gagné, J., Faherty, J. K., Cruz, K. L., et al. 2015, ApJS, 219, 33
Gagné, J., Mamajek, E. E., Malo, L., et al. 2018, ApJ, 856, 23
Gaia Collaboration, Brown, A. G. A., Vallenari, A., et al. 2021, A&A, 649, A1
Gioia, I. M., Maccacaro, T., Schild, R. E., et al. 1990, ApJS, 72, 567
Głębocki, R., & Gnaciński, P. 2005, in ESA SP-560, 13th Cambridge Workshop on Cool Stars, Stellar Systems and the Sun, ed. F. Favata, G. A. J. Hussain, & B. Battrick (Noordwijk: ESA), 571
Glebocki, R., & Gnacinski, P. 2005, yCat, III/244
Gossage, S., Conroy, C., Dotter, A., et al. 2018, ApJ, 863, 67
Greco, J. P., & Brandt, T. D. 2016, ApJ, 833, 134
Groff, T. D., Chilcote, J., Kasdin, N. J., et al. 2016, Proc. SPIE, 9908, 99080O
Holmberg, J., Nordström, B., & Andersen, J. 2009, A&A, 501, 941
Husser, T.-O., Wende-von Berg, S., Dreizler, S., et al. 2013, A&A, 553, A6
Jovanovic, N., Guyon, O., Martinache, F., et al. 2015, ApJL, 813, L24
Jovanovic, N., Martinache, F., Guyon, O., et al. 2015, PASP, 127, 890
Keppler, M., Benisty, M., Müller, A., et al. 2018, A&A, 617, A44
Kervella, P., Arenou, F., Mignard, F., & Thévenin, F. 2019, A&A, 623, A72
Konopacky, Q. M., Rameau, J., Duchêne, G., et al. 2016, ApJL, 829, L4
Kuzuhara, M., Tamura, M., Kudo, T., et al. 2013, ApJ, 774, 11
Kuzuhara, M., Currie, T., Takarada, T., et al. 2022, ApJL, 934, L18
Li, Y., Brandt, T. D., Brandt, G. M., et al. 2021, AJ, 162, 266
Macintosh, B. A., Graham, J. R., Barman, T. S., et al. 2015, Sci, 350, 64
Mamajek, E. E., & Hillenbrand, L. A. 2008, ApJ, 687, 1264
Marois, C., Doyon, R., Racine, R., & Nadeau, D. 2000, PASP, 112, 91
Marois, C., Lafreniere, D., Doyon, R., Macintosh, B., & Nadeau, D. 2006, ApJ, 641, 556
Marois, C., Lafrenière, D., Macintosh, B., & Doyon, R. 2008, ApJ, 673, 647
Marois, C., Macintosh, B., Barman, T., et al. 2008, Sci, 322, 1348
Marois, C., Zuckerman, B., Konopacky, Q. M., Macintosh, B., & Barman, T. 2010, Natur, 468, 1080
Mawet, D., Milli, J., Wahhaj, Z., et al. 2014, ApJ, 792, 97

Millar-Blanchaer, M. A., Perrin, M. D., Hung, L.-W., et al. 2016, Proc. SPIE, 9908, 990836
Miskovetz, K., Dupuy, T. J., Schonhut-Stasik, J., & Stassun, K. G. 2022, RNAAS, 6, 8
Montesinos, B., Gimenez, A., & Fernandez-Figueroa, M. 1988, MNRAS, 232, 361
Nielsen, E. L., De Rosa, R. J., Macintosh, B., et al. 2019, AJ, 158, 13
Nordström, B., Mayor, M., Andersen, J., et al. 2004, A&A, 418, 989
Norris, B., Schworer, G., Tuthill, P., et al. 2015, MNRAS, 447, 2894
Pecaut, M. J., & Mamajek, E. E. 2013, ApJS, 208, 9
Preibisch, T., Kim, Y.-C., Favata, F., et al. 2005, ApJS, 160, 401
Prusti, T., de Bruijne, J. H. J., Brown, A. G. A., et al. 2016, A&A, 595, A1
Pueyo, L. 2016, ApJ, 824, 117
Ricker, G. R., Winn, J. N., Vanderspek, R., et al. 2015, JATIS, 1, 014003
Salama, M., Ziegler, C., Baranec, C., et al. 2022, AJ, 163, 200
Skrutskie, M. F., Cutri, R. M., Stiening, R., et al. 2006, AJ, 131, 1163
Soummer, R., Pueyo, L., & Larkin, J. 2012, ApJL, 755, L28
Stanford-Moore, S. A., Nielsen, E. L., De Rosa, R. J., Macintosh, B., & Czekala, I. 2020, ApJ, 898, 27
Steiger, S., Bailey, J. I., III, Zobrist, N., et al. 2022, arXiv:2203.01406
Steiger, S., Currie, T., Brandt, T. D., et al. 2021, AJ, 162, 44
Thalmann, C., Carson, J., Janson, M., et al. 2009, ApJL, 707, L123
van Leeuwen, F. 2007, A&A, 474, 653
Vigan, A., Fontanive, C., Meyer, M., et al. 2021, A&A, 651, A72
Walter, A. B., Fruitwala, N., Steiger, S., et al. 2020, PASP, 132, 125005